Open Access
Recent Progress in Materials

Original Research

Toward Next Generation Plasmonic Nanopore Slit Platform with a ~10 nm Slit-Width

Seong Soo Choi [1, *], Byung Seong Bae [2], Kyoung Jin Kim [1], Myoung Jin Park [1], Yong Min Lee [1], Hyun Tae Kim [3], Soo Bong Choi [3]

1. Research Center for Nano-Bio Science, SunMoon University, Tangjung-Myun Sunmoon-Ro 221-70, Ahsan, Korea; E-Mails: sscphy2010@gmail.com; kjkim@sunmoon.ac.kr; mjpark.park@gmail.com; ymlee@sunmoon.ac.kr
2. School of Electronics and Display Engineering, Hoseo University, Ahsan, South Korea; E-Mail: bsbae3@hoseo.edu
3. Department of Physics, Incheon National University, Incheon, South Korea; E-Mails: htkim27@inu.ac.kr; sbchoi@gmail.com

* **Correspondence:** Seong Soo Choi; E-Mail: sscphy2010@gmail.com

Academic Editor: Georgia Paraskevi Nikoleli

Special Issue: Nanosensors: Recent Advances and Future Trends

Recent Progress in Materials
2021, volume 3, issue 1
doi:10.21926/rpm.2101004

Received: December 22, 2020
Accepted: January 26, 2021
Published: February 05, 2021

Abstract
We fabricated various nanoaperture plasmonic platforms for single-molecule detection. We fabricated nanoapertures like nanopores on a pyramid and nanoslits on an Au flat membrane using a Ga ion focused ion beam drilling technique, followed by irradiating with a high energy electron beam, dependent on the electron beam current density to obtain nanoapertures with a few nanometer sizes (circular nanopore, nanoslit pores). We examined their optical characteristics with varying aperture sizes and sample thicknesses. We obtained broad emission spectra in the visible and infrared region from the (7 x 7) slit array and a sharp, strong infrared emission peak from the Au nanoparticle on the substrate. The fabricated Au platform with ~10 nm nanometer opening can be employed as a single-molecule sensor and an infrared thermal emission device.

Keywords

Au nanoaperture; intraband; interband emission; surface plasmon; transmission electron microscopy; focused ion beam technique

1. Introduction

There have been tremendous interests in nanoapertures for single-molecule detection since DNA translocation and analysis via the natural nanopore (alpha-hemolysin nanopore) was carried out [1]. However, due to the negligible optical intensity through the tiny nanoaperture, plasmonic optical enhancement is required either by plasmonic hot spot or pattern-grooving and periodic arrays [2-7]. Recently, a SiN nanopore surrounded with Au nanowell with ~ 100 nm diameter was fabricated [8] due to the difficulties in fabrication of the nanometer-sized metallic apertures.

The Au nanopore formation, using a diffusion technique, with a diameter of ~ 5 nm was also reported [3-7] and using a drilling technique with high-energy electron beam irradiation [9]. The fabricated Au nanopore slit array with ~ 10 nm slit width can be utilized as a portable optical detection device for single-molecule analysis.

The fabrication of the nanoapertures with periodic groove patterns was reported to enhance the optical intensity through the tiny aperture [3-6, 9]. The pyramidal probe has been found to provide excellent light confinement inside a V-shaped cavity and enhanced optical throughput via cavity resonance and nanofocusing [3, 8-11]. Hence, the metallic nanostructure with an inverted pyramidal pit array would provide the immensely enhanced optical intensity for surface plasmonic Raman spectroscopy (SERS) [12]. We previously reported the SERS intensity enhancement using biolinker 1,2-Di(4-pyridyl)ethylene on the nanopatterned pyramidal probe [9].

Circular-type nanopore formation on pyramidal apices using focused Ga ion beam milling techniques followed by electron beam irradiations under high energy electron beam techniques has also been reported [3-7]. Upon high energy Ga ion impingement on the sample surface, atomic mixing occurs in the melted region within picoseconds, the ions diffuse, followed by the nanopore formation. This phenomenon can be ascribed to the thermal spike model [7, 13, 14]. During high energy ion beam impingements, the pore closing would occur due to the formation of a stressed viscous surface layer from high thermal temperature and atomic transport to the pore or mobile surface atom diffusion to the pore.

Fabrication of a circular-type nanopore with its diameter ranging from ~3 nm to ~10 nm using various surface modifications was reported [3, 4, 6-7, 9]. Ostwald ripening and spinodal decomposition on the diffused membrane were also observed under high-intensity electron beam irradiation [9]. It is generally understood that, for the samples with their aperture diameter smaller than the aperture thickness, the Au and C atoms diffuse inside the aperture, and it shrinks and forms the nanopore diffused with Au atoms and C atoms [4-7]. However, when the aperture diameter is larger than the aperture thickness, diffusion of Au and C atoms never occurs for TEM electron beam treatments. On the contrary, for the electron beam irradiations using FESEM, the aperture always shrinks regardless of the ratio of the aperture diameter to the aperture thickness. It may be attributed to the fast solid-state diffusion under very high electron beam probe current density of

1 nA/nm^2 for FESEM and to the liquid state equilibrium under electron beam irradiations with its current density ranging from ~10^2 pA/cm^2 to a few pA/cm^2 using TEM [4-7].

Growth of Au nanoparticles in nature was reported to have five body structures; the tetrahedron, the cube, the octahedron, the pentagonal dodecahedron, the icosahedron, as proposed by theory of five geometrical body structures in nature by Greek Philosopher, Plato. The faces of Plato's polyhedral are triangles, squares, and pentagons. Later, Kepler was inspired by observing the growth and the shape of pomegranate seeds and constructed the highly symmetric rhombic polyhedral [15]. The vacuum-deposited gold film consists of nanoparticles and multiple twin particle clusters with various shapes and sizes, of decahedron shape and icosahedron shape such as multiple twin particles (MTP) with a decahedron shape and an icosahedron shape [16-17]. Irregular variation of melting temperature for Au nanoparticles would present experimental difficulties for reproducible results [18, 19]. Au clusters with magic numbers are stable with higher melting temperatures than those of the usual nanoparticles [19-21].

During the electron beam irradiation on a thick specimen, a rise in its local temperature can be easily achieved, for high-energy electron beam irradiation, using FESEM or TEM. Widening or the closing (shrinking) may occur depending upon the viscosity of the heated membrane and the surface tension force, and the vapor pressure of the material [3-7, 22, 23]. Also, because graphene is a 2D sheet of carbon atoms and the carbon-graphite filter membrane consists of a periodic layer-by-layer slit structure with ~5 nm gap [24, 25], the Au nanopore slit array containing carbon atoms could be an excellent candidate for the plasmonic nanoaperture platform. For nanoscale double slits, the surface plasmonic wave from the nanoslits can provide the periodic interference phenomena for the TM wave between the nanoscale slits, which reduces or enhances the intensity of the far-field [26-28]. With proper control of the circular aperture pitch and the nanoscale slits separation gap, the optical intensity can be enhanced.

Fabrication of plasmonic nanopore on a pyramid and nanoscale double slits is previously investigated [5-7, 29-31]. It is reported that the light transmission through a conical type aperture is dependent on the polarization and aperture size for ka << 1, where k is the wave vector while a is the radius of the circular aperture [32, 33]. Lord Raleigh developed the theory of diffraction by a small nanoparticle and found that the far-field optical emission profile cannot distinguish its shape because light cannot recognize the particle with a size much smaller than the wavelength [34]. This theory can be applied for the nanoaperture with its size much smaller than the wavelength, combining the Babinet principle [35]. Besides, with decreasing aperture size, the diffracted angle increases, and the intensity profile becomes broader even with a backward scattering up to ~40% for the conical aperture diameter of 60 nm [32]. Furthermore, for the conical aperture diameter of 60 nm and P-polarized beam, backward scattering of the incident beam from the aperture is theoretically presented using quasi-multiple dipole approximation and can be attributed to a Poynting vector flow along the pyramidal surface of the aperture on the pyramidal apex [33].

Surface plasmon (SPP) mediated intraband emission, and the SPP-coupled transmission peaks with incoming waves dependent on the size of the nanoaperture and the sample thickness are reported [36]. The intraband optical peak at 500 nm is shown on the 180 nm thick Au films with and even without a single hole with ~250 nm diameter. Visible emissions are generated from the interband transitions of the d-band electrons into the conduction band followed by radiative recombination, and the strong infrared emission has resulted from the intraband transitions mediated by the confined fields near metal nanostructures (localized surface plasmons) [37].

Localized surface plasmon generates an emission peak in the infrared region due to the intraband transitions between conduction band states [37, 38]. The spatial confinement and coupling of the near-field results in an increase in the contribution of higher-order transition moments such as the electric quadrupole and octupole. Hence, the radiative intraband transitions in the conduction band can be allowed to cause the near-infrared emission observation of the nanostructures.

The strongly confined fields near gold nanostructures like a nanoslit array with a tiny ~10 nm opening width can also generate emission peaks in the infrared region due to the intraband transitions between conduction band states. The strong emission spectra in the visible range from the tiny apertures with various shapes can be utilized for single-molecule detection and analysis. Additionally, near-infrared emission, generated by nanoslits, can also be utilized for the far-field emitters and possible nearfield thermal cooling [39, 40]. In this report, we will demonstrate the fabrication of various nanoaperture platforms with a circular-type aperture and a nanoslit-type array and their optical characterizations.

2. Materials and Methods

Two types of Au nanoaperture platforms will be designed and fabricated: Nano-aperture array on the pyramid and flat membrane. First, we carried out the fabrication of nanometric size aperture arrays on top of oxide pyramids using conventional Si microfabrication techniques as in Figure 1(a)-1(f). Additionally, TEM grid samples with (100 μm x 100 μm) SiN membranes were also purchased from TEMwindows Company (www.temwindows.com), followed by the physical vapor deposition of Au thin films and dry etching of the supporting SiN film, depending upon the experimental conditions. After bulk Si etching on the backside of the Si wafer using TMAH solution, a (10 x 10) oxide pyramidal array is presented in Figure 1(g), and a side view of the single oxide pyramid is given in Figure 1(h). A circular oxide aperture on top of the pyramid is shown, occurring due to stress-dependent oxide growth on the pyramidal apex and slow isotropic etching of the SiO_2 as in Figure 1(i). Then, deposition of 200 nm Au thin film was performed using a thermal-deposition system. It was followed by 30 keV Focused Ga Ion Beam (FIB) drilling with the Focused Ion beam instrument (FEI Helios NanoLab Dual Beam system) and high energy electron beam irradiations using Field Emission Scanning Electron beam Microscopy (FESEM) and Transmission Electron beam Microscopy (TEM). TEM (JEM-2010 and JEM-3011 HR), FESEM (JSM 6400) were utilized at National Nation Fabrication Center (NNFC) in Daejeon, Korea. The optical spectra in the visible range were obtained using the Nikon Optical Eclipse Ti-U microscope with Princeton Instruments spectrophotometer (Acton SpectroPro 2300i, 150 g/mm). Besides, a solid-state Nd:YAG laser system with a wavelength of 532 nm as a light source and a silicon photosensor with a 15 mm cone attenuated F-filter (spectral range: 400 nm to ~1064 nm) for photodetection using a Witec SNOM instrument were used in the experimental setup. The minimum detection limit is of the order of 1 nW ($\sim 8.0 \times 10^{-10}$ W). The detailed schematics of the optical measurements are provided in the [Figure S1].

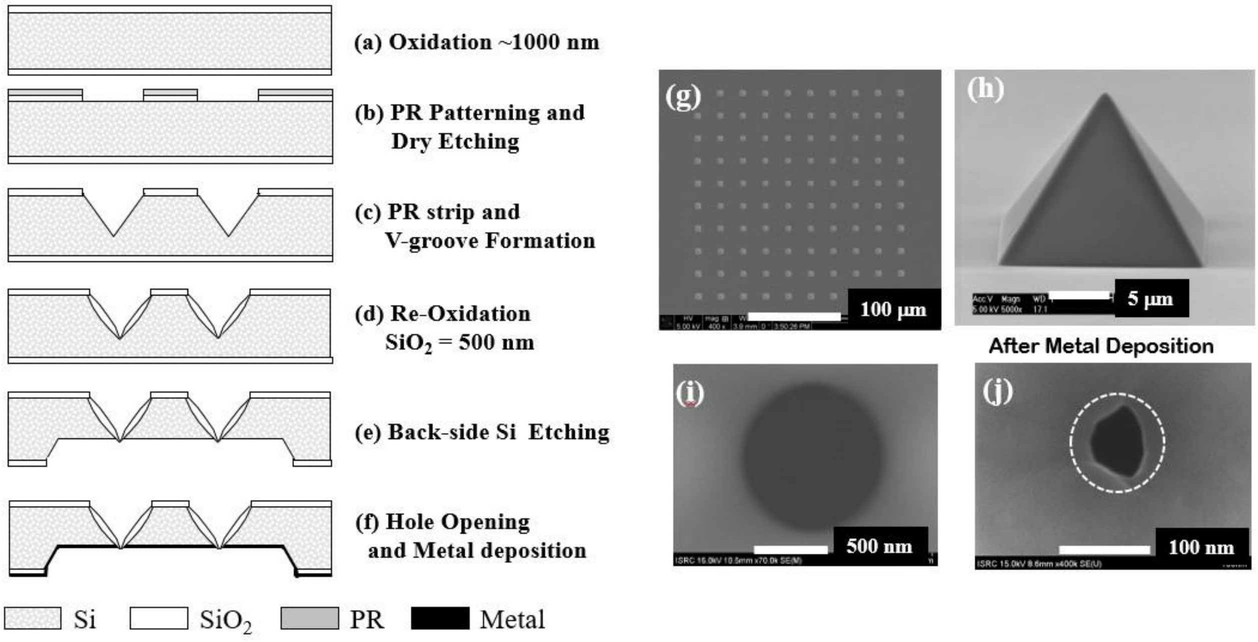

Figure 1 Fabrication schematics of the nano-apertures: Figure 1 (a)-(f). Figure 1(g) shows the (10x10) pyramidal array, and a FESEM image of the side view of the single pyramid is shown in Figure 1(h). FESEM images of the circular hole at the top of the pyramid after the TMAH bulk etching are presented in Figure 1(i), and the nanoaperture after Au thermal deposition is shown in Figure 1(j).

3. Results

We have fabricated the nanoapertures on a flat membrane and a pyramid, deposited by Au thin film, followed by 30 keV Ga ion focused ion beam milling. Fabrication of a circular aperture, with its diameter of 100 nm or less, is rather difficult due to an unstable focused ion beam during milling processing. Drilling the circular aperture with a 100 nm diameter or smaller would result in an elliptical aperture. To reduce the aperture size down to a few nanometer diameter after FIB drilling, we carried out two-step electron beam irradiations: (i) an electron beam irradiation of ~1 nA, at 2 keV using FESEM, (ii) electron beam irradiations with a current density ranging from ~10^0 to 10^2 at ~ 10^2 keV using TEM microscope. In this report, circular apertures with ~200 nm or greater diameter are initially fabricated on the 200 nm thick Au film. Then, to reduce the size of the circular-type Au aperture down to ~50 nm diameter, a 1.4 nA electron beam irradiation at 2 keV for 10 sec was employed using the field emission scanning electron beam instrument installed at Dual Beam Helio (FEI), followed by the high energy electron beam irradiation by using TEM. We also fabricated the nanoslit array with its opening width ranging from 100 nm to ~ 10 nm using 30 keV Ga FIB. The plasmonic effect from the nanoslit array is well known [29-31]. Nanoslit fabrication with an opening less than 50 nm is much easier than the circular-type aperture with a diameter of 50 nm or less.

3.1 Pore Formation Process Mechanism: Influence of the High Energy Electron Beam Irradiation

We investigated pore formation on the FIB drilled Au aperture under the influence of a high energy electron beam irradiation using TEM (JEM-2010, JEM-3011 HR). Figure 2(a) shows a nanopore with a diameter of 55.75 nm on the gold diffused membrane mixed with carbon atoms after the 2 keV FESEM electron beam irradiation. For the aperture, with a diameter greater than its thickness, it would not shrink even with high energy electron beam irradiation at 300 keV TEM. However, for electron beam irradiation using FESEM, Au atoms on the surface diffuse into the aperture, then form the nanopore on the diffused Au membrane mixed with carbon atoms. Therefore, we applied a two-step process for the pore formation for FIB drilled Au aperture with a ~ 279.5 nm diameter.

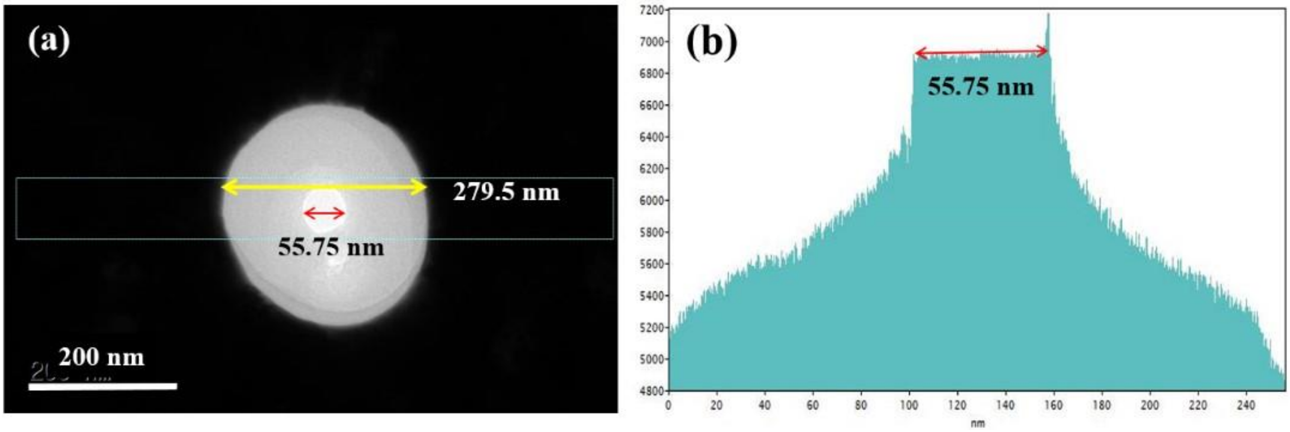

Figure 2 A ~279.5 nm diameter circle was initially drilled on a 200 nm thick Au flat film by 30 keV Ga ion beam followed by high energy electron beam irradiation at 2 keV, 1.4 nA FESEM electron beam irradiation for 10 sec. A TEM image of the 55.75 nm diameter nanopore on the Au diffused membrane 2(a). An electron beam intensity profile at the electron detector displays the 55.75 nm diameter of the formed nanopore on the diffused Au membrane mixed with carbon atoms 2(b).

3.1.1 Pore Formation on the Aperture with a Diameter Bigger than the Aperture Thickness

Figure 3 exhibits the pore shrinkage under successive electron beam irradiations for 50 min. For the 1st and 2nd electron beam irradiations for 10 min and 20 min, respectively, the pore shrinks from 55.75 nm to 30.79 nm, then to 20.97 nm. However, the pore shrinking rate becomes slower; for the 3rd, 4th, and 5th 10 min-electron beam irradiation, from 20.97 nm to 7.96 nm, to 5.79 nm, and down to 4.20 nm, respectively. The pore shrinking rate at 5th electron beam irradiation is ~0.159 nm/minute.

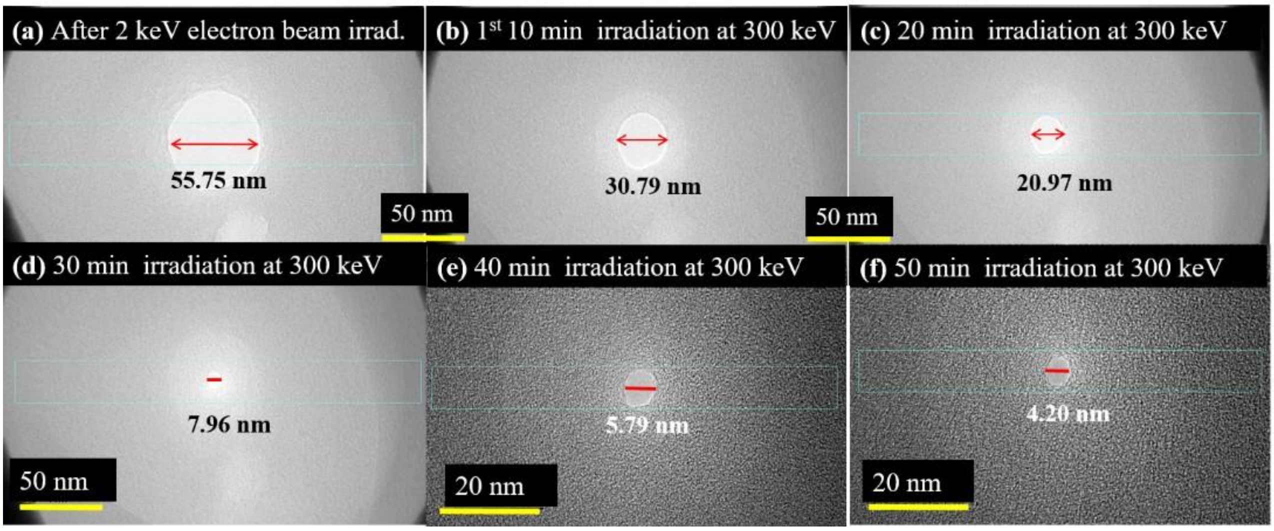

Figure 3 Successive electron beam irradiations with a 10 min-interval performed under 3 pA/cm^2 low current density of high energy electron beam irradiation at 300 keV TEM (JEM-3011 HR). A TEM image of a 55.75 nm diameter nanopore on the Au-C diffused membrane is presented, Fig. 3(a). A nanopore with a diameter of 55.75 nm was reduced to a smaller diameter nanopore of 30.79 nm, 20.97 nm, 7.96 nm, 5.79 nm, and 4.20 nm for 10 min, 20 min, 30 min, 40 min, and 50 min, respectively.

3.1.2 Pore Formation on the Aperture with a Diameter Smaller than the Aperture Thickness

Figure 4 presents the TEM images under the high energy electron beam irradiation on the FIB drilled Au aperture using a 200 keV TEM. For a designed diameter of 50 nm, we obtained an egg-shaped aperture (56.2 nm x 33.1 nm) due to the straggling of the focused Ga ion beam drilling process. Also, a pore of dimensions (22.2 nm x 25.7 nm) was formed on the Au-C mixed membrane inside a drilled Au (56.2 nm x 33.1 nm) aperture. Due to the thermal spike rise during a 30 keV FIB drilling process, Au atoms and C atoms diffuse simultaneously and form the thin membrane mixed with gold and carbon atoms, such that several Au particles and clusters on the Au-C diffused membrane form. A big Au particle (~10 nm diameter size of one particle on the left) (dashed red line) and another one on the right are shown in Figure 4(a). After 1st electron beam irradiation with 60.8 pA for 5 min, the (22.2 nm x 25.7 nm) pore reduced to (8.3 nm x 15.3 nm), Figure 4(b). After the 2nd 99.8 pA irradiation at 200 keV, the pore closed completely, and the diffusion of Au particles is seen clearly, Figure 4(c). After the 3rd 152.8 pA electron beam irradiation for 5 min, the diffused Au particle (13.5 nm diameter, inside the red dashed circle) became bigger than the one before electron beam irradiation, Figure 4(a). The diameter of the Au particle (~10 nm) before electron beam irradiation in Figure 4(a) became slightly bigger; the diameter of the Au particle was 13.5 nm as in Figure 4(d). The diffused membrane became thinner, the small particles became smaller, and the big particles became bigger. This phenomenon is because of Ostwald ripening. Please note that the large circular type particle (left side in Figure 4(a) was moved to the right and changed to an ellipsoidal shape particle (inside the dashed red inside in Figure 4(d)).

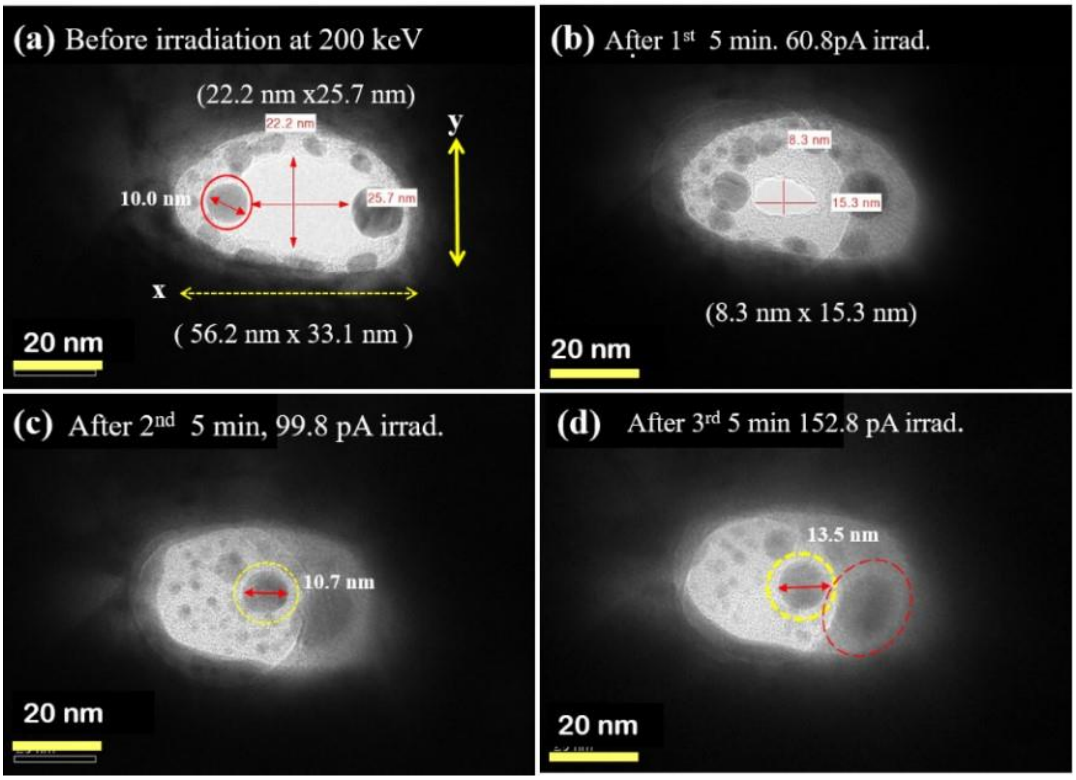

Figure 4 TEM images of nanopore under high energy electron currents at 200 keV (JEM-2010). A (56.2 nm x 33.1 nm) size Au aperture before irradiation (a), Reduced nanopore of (8.3 nm x 15.3 nm) under 1st 60.8 pA/cm^2 electron beam irradiation (b), a completely closed pore under 2nd 99.8 pA/cm^2 electron beam irradiation (c), thinned pore membrane under the very high intensity 152.8 pA/cm^2 for 5-minute irradiation (d). Several Au nanoparticles evaporated and became smaller along with thinning of the membrane, (c) and (d). Diffusion of 10 nm size Au nanoparticle under 60.8 pA/cm^2 electron beam irradiation, (b) and (c).

3.2 Optical Characteristics for the Fabricated Nano-Aperture Platforms: Nano-Slits Array and Nanopores on Pyramid

3.2.1 Nanoslit Array on ~130 nm Thick Au Film with Various Slit Sizes

Four different types of optical platforms are fabricated on ~130 nm Au film as in Figure 5; a (7 x 7) circular type aperture array with a ~100 nm designed diameter, two (7 x 7) slit arrays with a (100 nm wide x 500 nm long) slit size, (7 x 7) slit array with a (~40 nm wide x 500 nm long) slit size. The (x, y) pitch of the circular type aperture and the slit array are designed as (1 µm, 1 µm) and (550 nm, 500 nm), respectively, in Figure 5(a) and Figure 5(b). The measured pitches for the slit array pitch are (~532 nm, ~471 nm), in Figure 5(b). The (~40 nm wide x ~500 nm long) slit with tiny Au clusters and particles on the diffused membrane formed during Ga ion beam milling is also shown in Figure 5(c). The corresponding electronic profile for the width of the slit is in Figure 5(d).

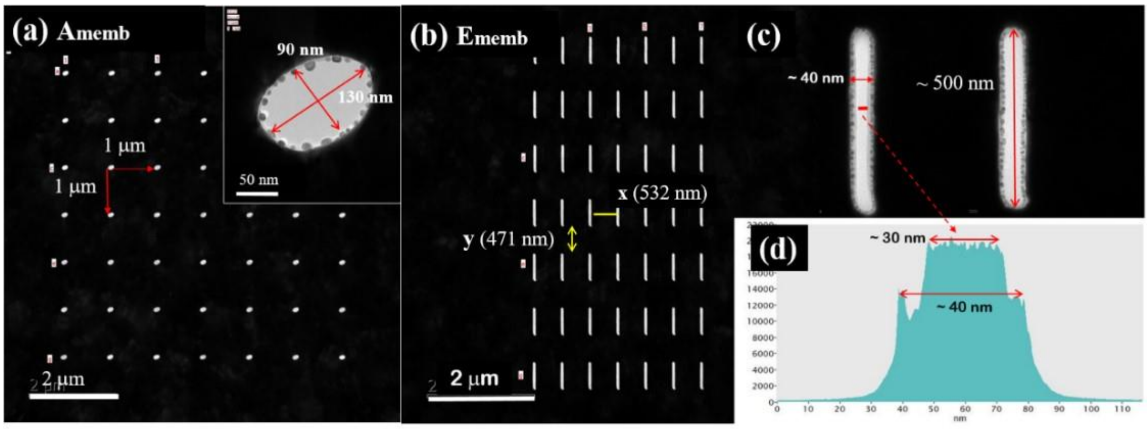

Figure 5 TEM images of the circular type aperture with a size of (130 nm x 90 nm) and a nanoscale slit array (~40 nm wide x ~500 nm long). The (x, y) pitches of the (7 x 7) circular type array and (7 x 7) nanoslit array are (~1 μm x 1 μm) and (532 nm x 471 nm), respectively. The TEM image of the nanoslit and the corresponding electronic profiles: (c) and (d).

Figure 6 presents the optical emission profiles from 4 nanoaperture platforms. All four nanoapertures have sharp optical spectra centered at ~500 nm, possibly due to the SPP-mediated intraband emission. The two (7 x 7) nanoslit arrays with 100 nm widths (G membrane and H membrane) present identical small SPP-coupled transmission peaks centered at ~671.5 nm. However, the nanoslit array with ~40 nm width (F membrane) presents a smaller shoulder profile at ~665 nm than those from (G and H). Moreover, the optical emission profile from A membrane with a (7 x 7) circular type array with a (~ 130 nm x ~ 90 nm) aperture size presents a sharp emission peak at ~500 nm with a negligible shoulder at ~650 nm.

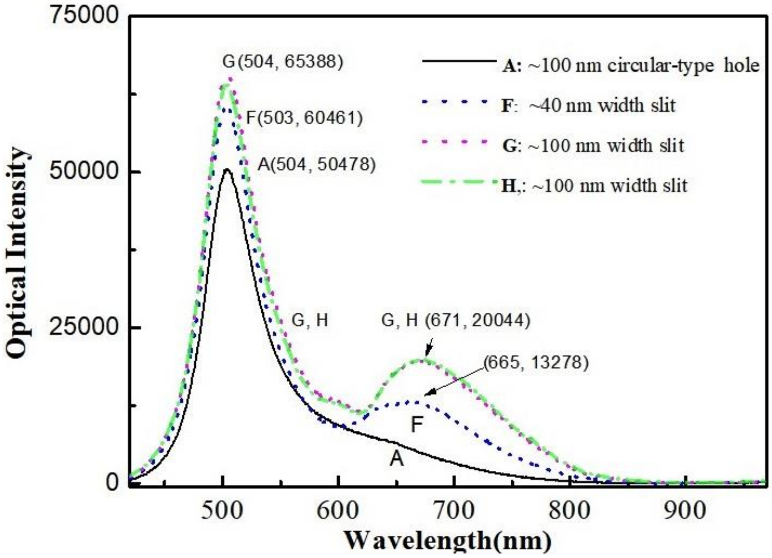

Figure 6 Optical characteristics of the (7 x 7) nanoslit array. A solid black line (A: a (7 x 7) circular type aperture array with a single aperture size of (~130 nm x ~90 nm)), a dotted blue line (F: slit size with 500 nm long and 40 nm wide), a red dash-dot red line (G: slit size with 500 nm long and 100 nm wide), and a green dash-dotted line (H: 500 nm long and 100 nm wide)

3.2.2 Nanopores on Pyramids with ~10^2 nm Aperture sizes

The nanoapertures on a pyramidal array are fabricated using Si microfabrication technique followed by metal deposition as in Figure 1. 5 TEM images are shown in Figure 7. In the dashed yellow circles in Figure 7(a) and 7(b), and a red dotted circle in Figure 7(c), the white area indicates an optically transparent nanopore region. The formed nanopores of the samples a3, a4, and a12 are measured to be (23 nm x 18 nm), (62 nm x 42 nm), (26.1 nm x 43.5 nm) on the thin membrane inside the apertures of (86.7 nm x 143 nm), (83.6 nm x 97.1 nm), and (111.8 nm x 152.7 nm), respectively. The nanoapertures of sample a15 and sample a19 are measured to be (112.5 nm x 130.4 nm), and (212.0 nm x 134.0 nm), respectively. The dark spots around the circumference of the aperture in Figure 7(a)-Figure 7(d) are Au clusters and numerous Au tiny particles (in the gray area in Figure 7(e)). The formation of Au nanoparticles and Au clusters on the gray membrane areas can be attributed to thermal spike during FIB drilling, and can also contribute to enhanced optical emission.

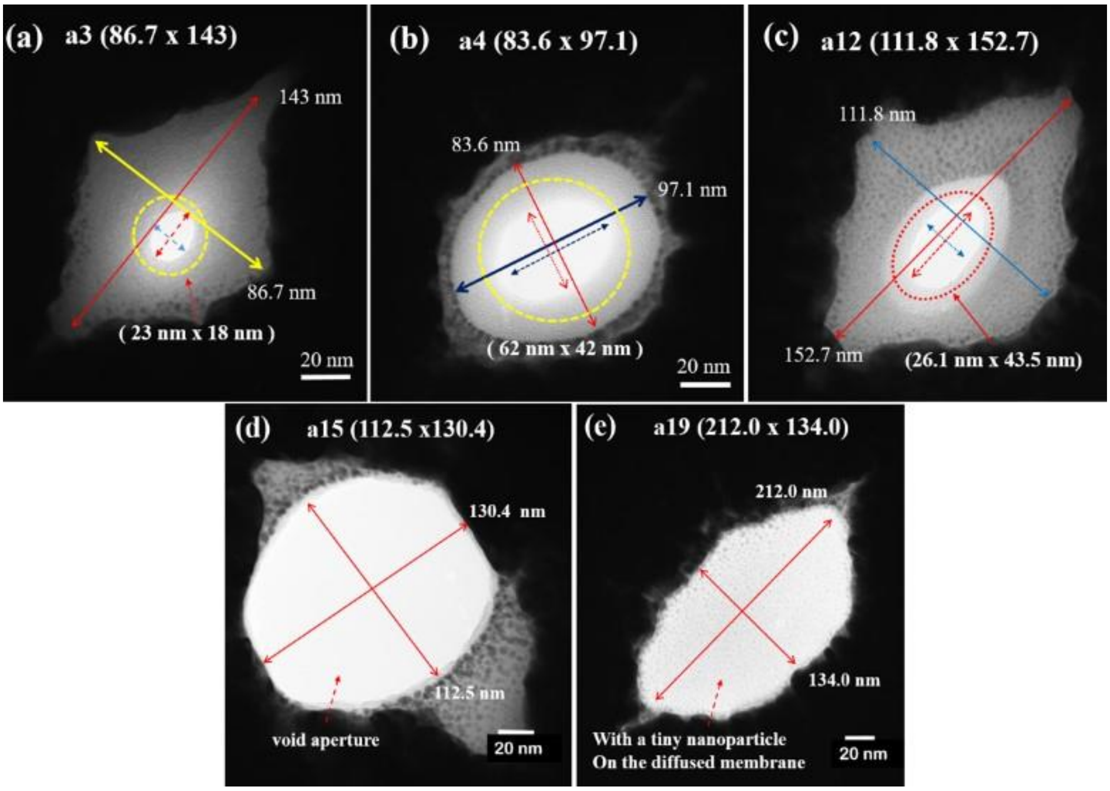

Figure 7 TEM images of nanopores and nanoapertures on pyramidal apices with a 200 nm thick Au film. The white pore areas inside the dotted circular gray area membrane are presented in (a), (b), and (c). The pore areas of a3, a4, and a12 are (23 nm x 18 nm), (62 nm x 42 nm), and (26.1 nm x 43.5 nm), respectively. The nanoapertures with sizes (112.5 nm x 130.4 nm) and (212.0 nm x 134.0 nm) are shown in (d) and (e), respectively. The diffused gray areas are the thin membranes composed of gold and carbon atoms in (d). Additionally, the tiny Au particles and clusters are present in the diffused dark gray area. However, the white aperture area also consists of small Au nanoparticles on the diffused thin membrane in panel (e).

Table 1 presents the optical output intensity against wavelengths by using a solid-state Nd:YAG laser system with a wavelength of 532 nm as a light source and a silicon photosensor with a 15 mm cone attenuated F filter (spectral range: 400 nm ~ 1064 nm) for photodetection using a Witec SNOM instrument. For the 532 nm input wavelength, the output intensities through the nanoapertures of samples a3, a4, a15, and a19 vary from 38.6 W to 48.3 W. The ratios for the samples a3, a4, a15, and a19 are of the order of ~3.1 x 10^{-2}, 3.1 x 10^{-2}, 2.6 x 10^{-2}, 3.3 x 10^{-2}, respectively. For 780 nm input wavelength, the output intensities through the nanoapertures of samples a3, a4, a15, and a19 are measured to be 8.4 W, 7.7 W, 6.7 W, 14.3 W, respectively, and the corresponding ratios are 0.36 x 10^{-2}, 0.33 x 10^{-2}, 0.28 x 10^{-2}, and 0.60 x 10^{-2}, respectively. These differences are attributed to higher excitation of photons at 532 nm input wavelength than at 780 nm and to the SPP-mediated emission peak at ~500 nm.

Table 1 Optical characteristics of the fabricated Au nanoapertures with sizes of a3 (~143 nm x ~ 86.7 nm), a4(~ 83.6 nm x ~ 97.1 nm), a15 (~112.5 nm x ~ 130.4 nm), and a19 (134.0 nm x 212.0 nm) are presented for the input wavelengths of 532 nm and 780 nm.

Sample ID	aperture size (nm^2)	Input wavelength (nm)	Input Intensity ($\mu W/cm^2$)	Output Intensity ($\mu W/cm^2$)	I_{out}/I_{in} ($x10^{-2}$)
a3	143 x 86.7	532	1477	45.7	3.1
a4	83.6 x 97.1			42.0	3.1
a15	112.5 x 130.4			38.6	2.6
a19	134.0 x 212.0			48.3	3.3
a3	143 x 86.7	780	2366	8.4	0.36
a4	83.6 x 97.1			7.7	0.33
a15	112.5 x 130.4			6.7	0.28
a19	134.0 x 212.0			14.3	0.60

The optical output intensity versus wavelength for samples a3, a4, a15, and a19 are presented in Figure 8. Optical characterization was performed using a Nikon Optical Eclipse Ti-U microscope with Princeton Instruments spectrophotometer (Acton SpectroPro 2300i, 150 g/mm) [Figure S2]. Input optical Gaussian beam intensity was calibrated using a (17 μm x 17 μm) square Si aperture. Output beam intensity profiles from sample a3 and sample a4 are presented in Figure 8(a). The areas of these particular samples of a3 and a4 are very close to each other, 7820 nm^2 and 6680 nm^2, respectively, and the ratio versus wavelength optical spectra are precise. Additionally, even with the 532 nm wavelength laser measurements, the ratios of the output to the input intensity are also the same; 3.1 x 10^{-2}. We observed the similar results from the sample a12, and a14 [Figure S3]. Two optical beam profiles have optical peaks at 568 nm and two inflection points- one at 511.8 nm and another at 675.2 nm. The point of inflection at 511.8 nm may be attributed to the intraband transition emission, and the point of inflection at 675.2 nm could be attributed to SPP-coupled incoming wave via nanoaperture. For sample a19, shown in Figure 8(b), the output optical peak

~595.8 nm with a broadened Gaussian shape between ~ 500 nm and ~ 700 nm are presented. The optical profile of sample a15, given in Figure 8(b), has a center point at 607.8 nm with broadband between ~524.8 nm and ~691.9 nm. Optical profile broadening with increased aperture size is agreeable with the previously published results [31, 32]. The SPP-coupled intraband optical emission would increase with the decreasing aperture diameter and the increasing surface wave along the pyramidal surfaces emanated from the aperture on the pyramidal apex.

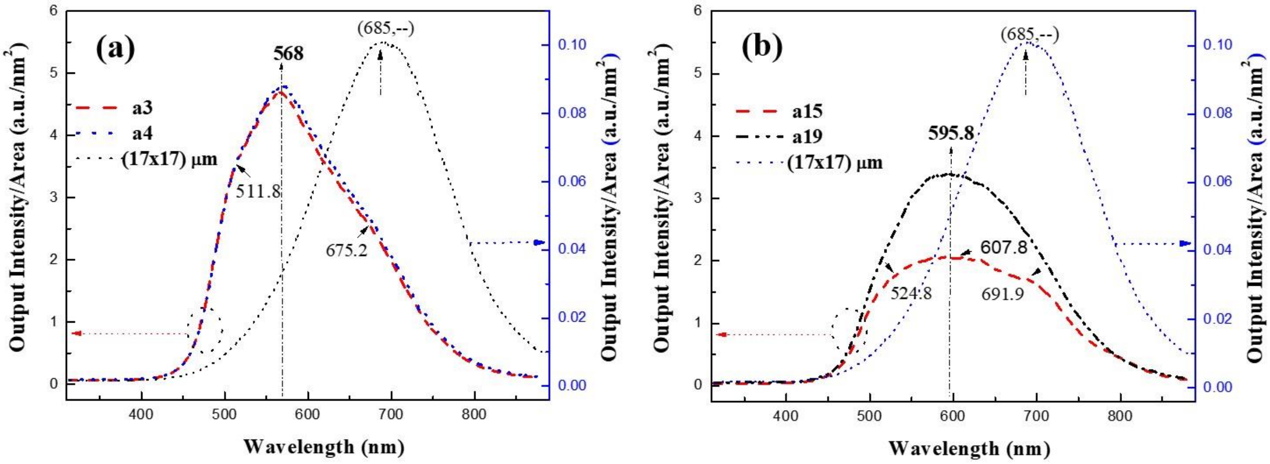

Figure 8 Normalized output optical intensities for Au apertures with optical Gaussian peaks at ~685 nm. For the Au apertures of a3 and a4 samples, the output spectra centered at ~568 nm and ~569 nm along with relatively sharp and narrow Gaussian-type shape spectra (a). Both transmitted optical profiles of sample a3 and sample a4 have optical peaks at ~568 nm with two points of inflection- one at ~511.8 nm and the other at ~675.2 nm. For a19 sample (b), the output optical peak is at ~595.8 nm with a broadened Gaussian shape between ~500 nm and ~ 700 nm. For sample a15, the profile has a center at ~607.8 nm with broadband between ~524.8 nm and ~691.9 nm. Input beam optical intensity was calibrated using (17 μm x 17 μm) aperture.

The ratio of output intensity to input intensity can provide information on the nanoapertures and their optical characteristics. Figure 9 presents the graph of the ratio of normalized output intensity to normalized input intensity versus wavelength. The sharp conical ratio profiles with the optical peaks at 497 nm and 499 nm for the sample a3 and a4 respectively are shown with slightly deviated to the right wavelength from the peak line at 497 nm. The asymmetrical profile presents: at the ratio value of 150, close to the half maximum, the corresponding wavelengths are 467.6 nm and 551.1 nm, not symmetrical from the peak. For samples a15 and a19, the profiles became broader and asymmetrical with a peak at ~500 nm. The contribution from the SPP-coupled wave with the incoming beam through the aperture may cause this asymmetrical profile.

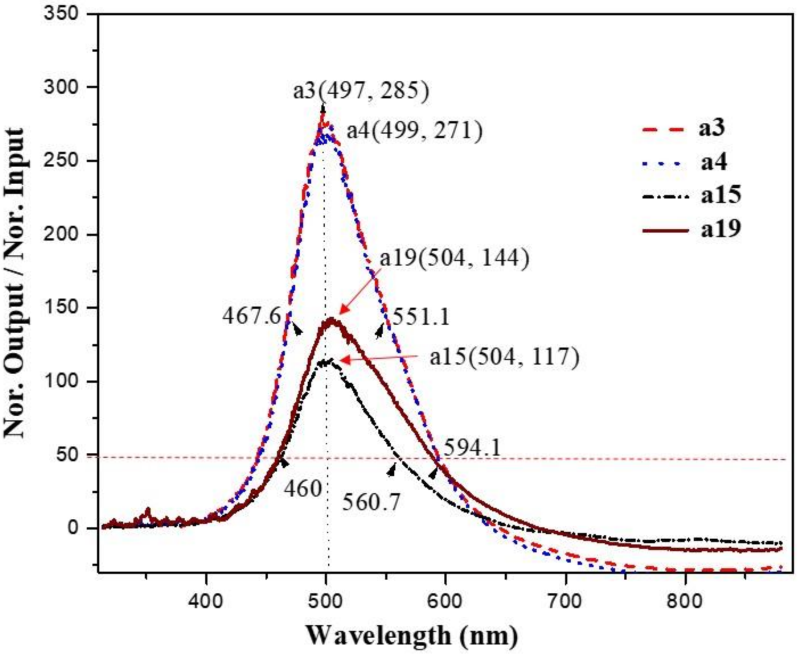

Figure 9 Plot of the ratio of normalized output intensity to normalized input intensity versus wavelength for samples a3, a4, a15, and a19. For samples a3 and a4, the ratio profiles present a conical shape centered at ~497 nm and ~499 nm, respectively. For samples a15 and a19, the ratio profiles are lower maxima with a greater full width half maximum (FWHM) than with a3 and a4 samples.

3.2.3 Fabrication of (7 x 7) Nanoslit Array with a (~10 nm x ~300 nm) Slit Size

We fabricated the (7 x 7) nanoslit arrays using 30 keV Ga ion FIB on the 200 nm thick Au on the supporting layer 20 nm SiN. Figure 10 (a) presents TEM images of the (~100 μm x ~100 μm)m membrane and the (7 x 7) nanoslit array with a (~3 μm x ~3 μm) size at the center of the A, C, E, and F membranes (inside a solid yellow circle). The (x, y) pitch is measured to be (500 nm, 250 nm) in Figure 10(c) and Figure 10(d). The size of each nanoslit is measured to be (~10 nm x ~300 nm). Figure 11 presents the TEM images of the slits with ~10 nm opening on the A membrane. TEM images for the E membrane are shown [Figure S3]. A FESEM image of an ~200 nm size Au particle on the C membrane and a TEM image of the (~7.2 μm x ~2.3 μm) size aperture on the F membrane are presented [Figure S4]. Figure 12 exhibits the measured optical characteristics for the four samples. The optical spectra ranging from ~450 nm to ~900 nm are shown along with small Gaussian shape emission peaks at ~500 nm. Two broad emission bands from sample A and sample E exhibit relatively flat broad bands with a plateau region from ~600 nm to ~850 nm. However, the emission band from E has greater intensities by double than those from sample A. The difference can be attributed to the different surface statuses between the two samples. The green strong peak at F (665.8) may be attributed to the SPP-coupling contribution from the small void aperture (~7.2 μm x ~2.3 μm) on the membrane. A red sharp infrared peak at C (769.1) can be attributed to the SPP-scattering from a ~200 nm size Au particle.

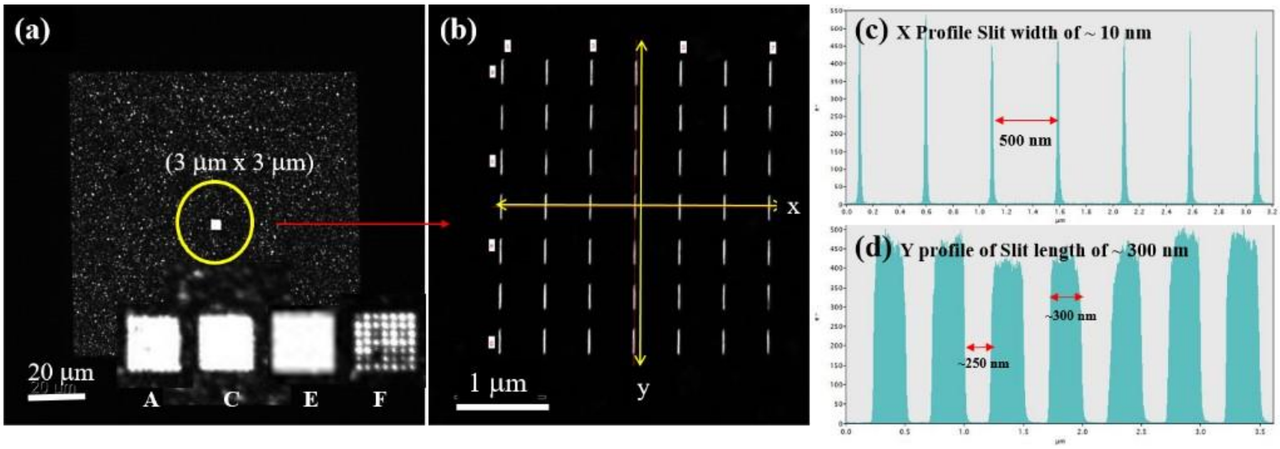

Figure 10 TEM images of the (~100 µm x ~100 µm) membrane and the (7 x 7) nanoslit array with (~3 µm x ~3 µm) at the center of the A, C, E, and F membrane (inside a solid yellow circle). The three white squares at the bottom indicate the nanoslit areas of A, C, and E membranes, and the gray square area with grids indicates the nanoslit in the F membrane. The (x, y) profiles at the electron beam detector were measured. The widths and the length of the slits are found to be ~10 nm and ~300 nm, respectively. The (x, y) pitches of the slit arrays are found to be (~500 nm, ~250 nm) in (c) and (d).

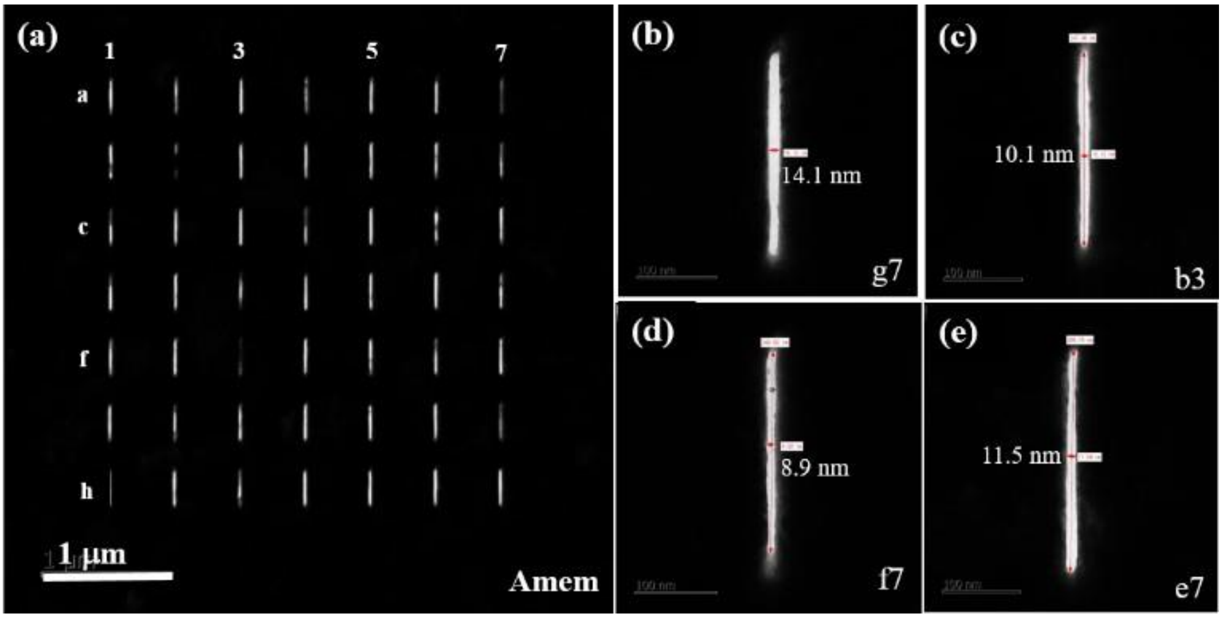

Figure 11 TEM images of sample A membrane for a (7 x 7) nanoslit array. Several dim nanoslits are also shown due to the diffusion of Au atoms during 30 keV Ga ion beam drilling. The slit widths of (g7, b3, f7, and e7) are measured to be 14.1 nm, 10.1 nm, 8.9 nm, and 11.5 nm, respectively.

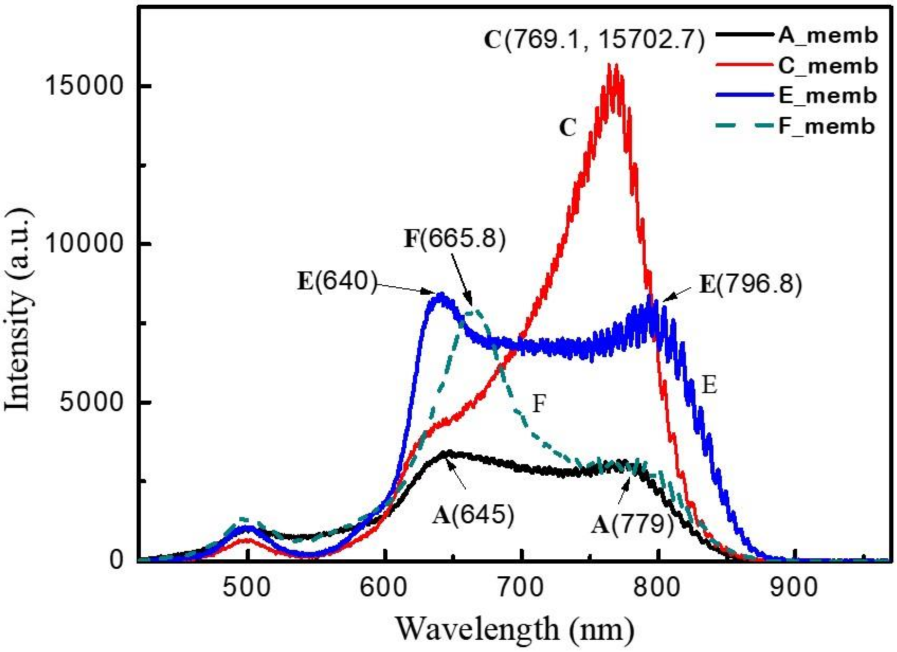

Figure 12 Optical characteristics of the (7 x 7) slit arrays. Optical emission spectra ranging from ~450 nm to ~900 nm with a small emission peak at ~500 nm. Two optical emission spectra from sample A and sample E present relatively flat broad bands (plateau region) from ~640 nm to ~800 nm. A strong emission peak at 665.8 nm from sample F (blue line) and a sharp peak at 769.1 nm from sample C (red line) can be attributed to the contribution from the beam transmitted through the hole on the F membrane and scattering from ~200 nm Au particle on the C membrane, respectively.

4. Discussion

(i) We investigated the influence of high-energy electron beam irradiation dependent on the aperture size. We performed two-step electron beam irradiations for the aperture greater than its thickness: 2 keV FESEM electron beam irradiation followed by electron beam irradiation at 3 pA, 300 keV TEM to obtain a nanopore of ~ 4 nm on the ~ 279.5 nm diameter Au aperture. For the apertures smaller than aperture thickness, higher electron beam currents of ~60 pA or more at 200 keV TEM were irradiated on the (56.2 nm x 33.1 nm) Au aperture on the 200 nm thick Au film to obtain the Au nanopore with its size of (8.3 nm x 15.3 nm). With the currents higher than 100 pA at 200 keV, pore closing and thinning of the formed membrane are observed due to diffusion of gold atoms and carbon atoms, sputtering of carbon atoms, and evaporation of Au atoms.

(ii) Au nanopores and apertures on the pyramidal apices with optical characterizations: Au pyramidal-apertures with sizes ranging from (143 nm x 86.7 nm) to (134 nm x 212 nm) were micro-fabricated). The observed output intensity peaks for the relatively small aperture areas of a3 (143 nm x 86.7 nm) and a4 (83.6 nm x 97.1 nm) and for the larger areas of the samples a15 (112.5 x 130.4 nm) and a19 (134.0 nm x 212.0 nm) are observed to be at 568.2 nm and 569.2 nm, and 596.5 nm and 592.7 nm, respectively. The Full Width Half Maxima (FWHM) for the optical spectra from the a3 sample and the a4 sample is much narrower than those for sample a15 and sample 19. The greater FWHM with the shifted peak to the higher wavelengths indicates the coupling with the incoming wave. Additionally, the ratio profiles also present a strong contribution from the SPP-mediated intraband emission at ~ 500 nm. The precise optical emission spectra along with the ratio profiles from sample a3 and the sample a4 can be attributed to Lord Raleigh's statement about the diffraction small particle and Babinet principle; the far-field emission does not depend upon the shape of the particle and the aperture for the small particle and aperture smaller than the wavelength. Moreover, optical profile broadening with increased aperture size is agreeable with the previously published results by Obermüller et al. With decreasing the aperture diameter, the increased SPP-coupled intraband optical emission is observed due to the increased surface wave along the pyramidal surfaces emanated from the aperture on the pyramidal apex. For the small apertures of the sample a3 and the sample a4, the conical type output optical profiles are shown with a peak at 568 nm; however, for the larger apertures of the sample a15 and the sample a19, the broad profiles are shown with the shifted peak position at 595.8 nm from input peak at 685 nm. The peak shift can be attributed to SPP-coupling from incoming optical beam through the nanoapertures and the possible scattering with Au particles and Au clusters. The detailed physical mechanism should be investigated further.

(iii) Optical characterization of the fabricated platforms with a (7 x 7) nanoslit array, or with a circular type hole array with a (90 nm x 130 nm) size on the 130 nm thick Au film: Regardless of the aperture types, either circular or slit, sharp optical peaks at ~500 nm are observed. For the nanoslit array with a slit dimension of (~100 nm x ~500 nm), a sharp conical type profile with its peak at ~500 nm and a broad profile with a small peak at ~671 nm are observed. Even though a sharp conical-shaped profile with a peak at ~500 nm is observed for the nanoslit array with a slit dimension of (~40 nm x ~500 nm), a smaller broad profile at 665 nm is also seen. No optical emission peak at ~670 nm is observed for this sample and a (7 x 7) circular type hole array with (~ 90 nm x ~ 130 nm) dimensions on the ~130 nm thick Au membrane.

(iv) The broad optical spectra ranging from 550 nm to 900 nm with a small optical peak at 500 nm were obtained from the (7 x 7) nanoslit array platforms, possibly contributed from the SPP-mediated intraband emission. The fabricated (7 x 7) nanoslit array consists of each slit with (~10 nm x ~300 nm) dimensions. The (x, y) pitch of the slit array is estimated to be (250 nm, 500 nm). The small optical peak at 500 nm can be attributed to the SPP-mediated intraband emission. The broad emission in the visible range can be due to the interband transitions of d-band electrons into the conduction band, and the emission in the infrared region is generated from the intraband transitions mediated by the strongly confined fields (localized surface plasmons) from the nanoslit array with ~10 nm slit opening.

5. Conclusions

We conclude the following:

(i) Depending on the aperture thickness and aperture diameter, pore-formation procedures should be varied.

(ii) Optical emission characteristics from various Au nanostructures are dependent on the film thickness and aperture size.

(iii) A strong contribution from SPP-mediated intraband for small apertures and a weak contribution from SPP-coupled transition for larger apertures are observed.

Acknowledgments

This work was supported by the research funding programs (Development of Biofriendly Optical Nanopore, 2018R1D1A1B07050106) under the Basic Science Research Program through the National Research Foundation (NRF) funded by the Ministry of Education, Science and Technology, South Korea.

Additional Materials

The following additional materials are uploaded at the page of this paper.

1. Figure S1: The following schematic diagram show the optical systems using 532 laser and Halogen lamp.
2. Figure S2: Pyramidal apertures with the a3 and a4, with a12 and a14.
3. Figure S3: (7x7) slit array Ememb.
4. Figure S4: FESEM image of an ~200 nm diameter Au nanoparticle on C membrane (left) and TEM image of a void aperture of (7.2 µm x 2.3 µm) size on the F membrane (right).

Author Contributions

Conceptualization, Choi, S.S. (nanofabrication); Kim, K.J. (single molecule detection); Park, M.J. (plasmonics); methodology, Bae B.S. (materials preparation); Kim, H.T.; Choi, S.B.; formal analysis, Choi, S.S.; Kim, H.T.; investigation, Choi, S.S.; resources; data curation, Bae B.S., Lee Y.M.; writing—original draft preparation, Choi, S.S.; writing—review and editing, Bae, B.S.; Park, M.J.; Lee, Y.M.

Funding

This work was supported by the research funding programs (Development of Biofriendly Optical Nanopore, 2018R1D1A1B07050106) under the Basic Science Research Program through the National Research Foundation (NRF) funded by the Ministry of Education, Science and Technology, South Korea.

Competing Interests

The authors have declared that no competing interests exist.

References

1. Howorka S, Cheley S, Bayley H. Sequence-specific detection of individual DNA strands using engineered nanopore. Nat Biotechnol. 2001; 19: 636-639.
2. Ebbesen TW, Lezec HJ, Ghaemi HF, Thio T, Wolff PA. Extraordinary optical transmission through sub-wavelength hole arrays. Nature. 1998; 391: 667-669.
3. Choi SS, Park MJ, Han CH, Oh SJ, Han SH, Park NK, et al. Fabrication of pyramidal probes with various periodic patterns and a single nanopore. J Vac Sci Technol B. 2015; 33: 06F203.
4. Choi SS, Park MJ, Han CH, Oh SJ, Yamaguchi T, Park NK, et al. Formation of an Au membrane incorporated with carbon atoms under electron beam irradiations. Surf Coat Technol. 2016; 306: 113-118.

5. Choi SS, Park MJ, Yamaguchi T, Han CH, Oh SJ, Kim SI, et al. Nanopore formation on Au coated pyramid under electron beam irradiations (plasmonic nanopore on pyramid). Sens Bio-Sens Res. 2016; 7: 153-161.
6. Choi SS, Park MJ, Yamaguchi T, Kim SI, Park KJ, Park NK. Fabrication of nanopore on pyramid. Appl Surf Sci. 2014; 310: 196-203.
7. Choi SS, Oh SJ, Han CH, Park DJ, Choi SB, Kim YS, et al. Au cluster formation on a pore-containing membrane under various surface treatments. J Vac Sci Technol B. 2017; 35: 04F107.
8. Garoli D, Yamazaki H, Maccaferri N, Wanunu M. Plasmonic nanopores for single-molecule detection and manipulation: Toward sequencing applications. Nano Lett. 2019; 19: 7553-7562.
9. Choi SS, Park MJ, Oh SJ, Han CH, Kim YS, Park NK. Plasmonic nanopore with nanopattern and nanoparticles for single molecule analysis. Phys Status Solidi A. 2017; 215: 1700484.
10. Vernon KC, Davis TJ, Scoles FH, Gómez DE, Lau D. Physical mechanisms behind the SERS enhancement of pyramidal pit substrates. J Raman Spectrosc. 2010; 41: 1106-1111.
11. Consoni M, Hazart J, Lérondel G, Vial A. Nanometer scale light focusing with high cavity-enhanced output. J Appl Phys. 2009; 105: 084308.
12. Radziuk D, Moehwald H. Prospects for plasmonic hot spots in single molecule SERS towards the chemical imaging of live cells. Phys Chem Chem Phys. 2015; 17: 21072-21093.
13. Bringa EM, Johnson RE. Coulomb explosion and thermal spikes. Phys Rev Lett. 2002; 88: 165501.
14. Howie A. Electron microscopy: Coulomb explosions in metals? Nature. 1986; 320: 684.
15. Martin TP. Shells of atoms. Phys Rep. 1996; 273: 199-241.
16. Komoda T. Study on the structure of evaporated gold particles by means of a high resolution electron microscope. Jpn J Appl Phys. 1968; 7: 27-30.
17. Pashlemy DW, Stowell MJ, Jacobs MH, Law TJ. The growth and structure of gold and silver deposits formed by evaporation inside an electron microscope. Philos Mag. 1964; 10: 127-158.
18. Ino S. Epitaxial growth of metals on rocksalt faces cleaved in vacuum. II. orientation and structure of gold particles formed in ultrahigh vacuum. J Phys Soc Jpn. 1966; 21: 346-362.
19. Buffat Ph, Borel JP. Size effect on the melting temperature of gold particles. Phys Rev A. 1976; 13: 2287-2298.
20. Li H, Li L, Pedersen A, Gao Y, Khetrapal N, Jónsson, H, et al. Magic-number gold nanoclusters with diameters from 1 to 3.5 nm: Relative stability and catalytic activity for CO oxidation. Nano Lett. 2015; 15: 682-688.
21. Schmidt M, Kusche R, von Issendorff B, Haberland H. Irregular variations in the melting point of size-selected atomic clusters. Nature. 1998; 393: 238-240.
22. Storm AJ, Chen JH, Ling XS, Zanbergen HW, Dekker C. Fabrication of solid-state nanopores with single-nanometre precision. Nat Mater. 2003; 2: 537-540.
23. Li J, Stein D, McMullan C, Branton D, Aziz MJ, Golovchenko JA. Ion-beam sculpting at nanometre length scales. Nature. 2001; 412: 166-169.
24. Trinh TT, Vlugt TJ, Hägg MB, Bedeaux D, Kjelstrup S. Simulation of pore width and pore charge effects on selectivities of CO_2 vs. H_2 from a syngas-like mixture in carbon mesopores. Energy Procedia. 2015; 64: 150-159.
25. Haque F, Li J, Wu HC, Liang XJ, Guo P. Solid-state and biological nanopore for real-time sensing of single chemical and sequencing of DNA. Nano Today. 2013; 8: 56-74.
26. Schouten HF, Kuzmin N, Dubois G, Visser TD, Gbur G, Alkemade PF, et al. Plasmon-assisted two-slit transmission: Young's experiment revisited. Phys Rev Lett. 2005; 94: 053901.

27. Gan CH, Gbur G, Visser TD. Surface plasmons modulate the spatial coherence in Young's interference experiment. Phys Rev Lett. 2007; 98: 043908.
28. Verma M, Joshi S, Bisht NS, Kandpal HC, Senthilkumaran P, Joseph J. Effect of surface plasmons on spectral switching of polychromatic light with Au-double-slit. J Opt Soc Am A Opt Image Sci Vis. 2012; 29: 195-199.
29. Choi SS, Park MJ, Han CH, Oh SJ, Kim HT, Choi SB, et al. Plasmonic nanopore fabrication for single molecule bio sensor using electron beam irradiation. ECS Trans. 2018; 85: 69-76.
30. Choi SS, Oh SJ, Lee YM, Kim HT, Choi SB, Bae BS. Fabrication of plasmonic optical nanopore platform for single molecule sensing. J Electrochem Soc. 2020; 167: 027503.
31. Choi SS, Park MJ, Lee YM, Bae BS, Kim HT, Choi SB. Fabrication of the Au nano-aperture array platform for single molecule analysis. ECS J Solid State Sci Technol. 2020; 9: 115015.
32. Obermüller C, Karrai K. Far field characterization of diffracting circular apertures. Appl Phys Lett. 1995; 67: 3408-3410.
33. Drezet A, Woehl JC, Huant S. Diffraction by a small aperture in conical geometry: Application to metal-coated tips used in near-field scanning optical microscopy. Phys Rev E. 2002; 65: 046611.
34. Lord Rayleigh FR. XXXVII. On the passage of waves through apertures in plane screens, and allied problems. London Edinburgh Dublin Philos Mag J Sci. 1897; 43: 259-272.
35. Babinet M. Mémoires d'optique météorologique. C R Acad Sci. 1837; 4: 638-648.
36. Gao H, Henzie J, Odom TW. Direct evidence for surface plasmon-mediated enhanced light transmission through metallic nanohole array. Nano Lett. 2006; 6: 2104-2108.
37. Beversluis MR, Bouhelier A, Novotny L. Continuum generation from single gold nanostructures through near-field mediated intraband transitions. Phys Rev B. 2003; 68: 115433.
38. Ebrahimpour Z, Mansour N. Plasmonic near-field effect on visible and near-infrared emissions from self-assembled gold nanoparticle films. Plasmonics. 2018; 13: 1335-1342.
39. Greffet JJ. Revisiting thermal radiation in the near field. C R Phys. 2017; 18: 24-30.
40. Baranov DG, Xiao Y, Nechepurenko IA, Krasnok A, Alù A, Kats MA. Nanophotonic engineering of far-field thermal emitters. Nat Mater. 2019; 8: 920-930.